Experimental Validation of Two-dimensional Finite Element Method for Simulating Constitutive Response of Polycrystals During High Temperature Plastic Deformation

Sumit Agarwal, Clyde L. Briant, Paul E. Krajewski, Allan F. Bower, and Eric M. Taleff

A finite element method was recently designed to model the mechanisms that cause superplastic deformation (A.F. Bower and E. Wininger, A Two-Dimensional Finite Element Method for Simulating the Constitutive Response and Microstructure of Polycrystals during High-Temperature Plastic Deformation, *J. Mech. Phys. Solids*, 2004, 52, p 1289–1317). The computations idealize the solid as a collection of two-dimensional grains, separated by sharp grain boundaries. The grains may deform plastically by thermally activated dislocation motion, which is modeled using a conventional crystal plasticity law. The solid may also deform by sliding on the grain boundaries, or by stress-driven diffusion of atoms along grain boundaries. The governing equations are solved using a finite element method, which includes a front-tracking procedure to monitor the evolution of the grain boundaries and surfaces in the solid. The goal of this article is to validate these computations by systematically comparing numerical predictions to experimental measurements of the elevated-temperature response of aluminum alloy AA5083 (M.-A. Kulas, W.P. Green, E.M. Taleff, P.E. Krajewski, and T.R. McNelley, Deformation Mechanisms in Superplastic AA5083 materials. *Metall. Mater. Trans. A*, 2005, 36(5), p 1249–1261). The experimental work revealed that a transition occurs from grain-boundary sliding to dislocation (solute-drag) creep at approximately 0.001/s for temperatures between 425 and 500 °C. In addition, increasing the grain size from 7 to 10 μm decreased the transition to significantly lower strain rates. Predictions from the finite element method accurately predict the effect of grain size on the transition in deformation mechanisms.

1. Introduction

Superplastic Forming (SPF) (Ref 1) and Quick Plastic Forming (QPF) (Ref 2) are hot blow forming processes, which enable complex shapes to be manufactured using fine-grained aluminum sheet alloys. SPF is traditionally performed at high temperatures (>500 °C) and slow strain rates (<0.001/s), where grain-boundary-sliding creep dominates deformation. QPF

Sumit Agarwal, Clyde L. Briant, and **Allan F. Bower,** Division of Engineering, Brown University, Providence, RI 02912; **Paul E. Krajewski,** General Motors R&D Center, 30500 Mound Rd, Warren 48090 MI; and **Eric M. Taleff,** Department of Mechanical Engineering, The University of Texas at Austin, 1 University Station C2200, 78712-0292 Austin, TX. Contact e-mail: Sumit_Agarwal@amat.com.

operates at lower temperatures (450 °C) and faster strain rates (>0.001/s), in a regime where both grain-boundary sliding and solute-drag creep contribute to plasticity. The alloy typically used for both processes in the automotive industry is AA5083, the deformation behavior of which has been well characterized (Ref 3–11).

While AA5083 has provided good performance in both SPF and QPF processes, improvements in formability could enable faster production rates and increase the opportunity for proliferation of the technology. Formability at elevated temperature is governed primarily by (i) strain-rate sensitivity which, when positive, delays strain localization and the onset of necking and (ii) nucleation and growth of cavities which coalesce and lead to failure. The strain-rate sensitivity is governed primarily by the dominant deformation mechanism; if creep occurs by grain-boundary sliding, the stress increases rapidly with strain rate, while a more gradual variation of stress with strain rate is observed in the dislocation creep regime. The deformation mechanism and the nucleation and growth of cavities are controlled by microstructural features, such as texture and texture evolution, grain size, dynamic grain growth, and constituent particle/dispersoid size, and distribution. Understanding the influence of these microstructural features on the deformation mechanisms and macroscopic constitutive behavior is an important step towards developing materials and microstructures with enhanced formability at elevated temperatures.

To this end, we have recently developed a finite element method that is intended to model the mechanisms of plastic flow during high-temperature straining of a polycrystalline alloy. The simulations account for the principal mechanisms that are believed to contribute to creep, including thermally activated dislocation creep within the grains; grain-boundary sliding, and grain-boundary diffusion. These calculations predict the distribution of stress and strain within the microstructure and can, therefore, be used to calculate the macroscopic constitutive behavior of the solid as a function of grain size, temperature, strain rate, and parameters governing microscopic mechanisms of deformation. In addition, the simulations predict the contribution to the total plastic strain rate from dislocation creep and grain-boundary sliding and, thus, can be used to predict transitions in the deformation mechanism. Finally, the simulations predict the evolution of the grain structure as a consequence of deformation, diffusion, and can also account for the influence of voids in the solid. They can, therefore, model damage and microstructure evolution during straining.

The goal in this paper is to systematically compare the predictions of these simulations with experimental measurements of the constitutive response and microstructure evolution of AA5083. Strain-rate-change tests were used to measure the steady-state stress as a function of strain rate under uniaxial tensile straining, for specimens with several grain sizes (Ref 12). In addition, the evolution of grain structure and texture were monitored by taking electron backscatter-diffraction images of specimens from tensile tests (Ref 13). The experimental response of stress to strain rate can be approximated by a standard power-law creep expression of the form $\dot{\varepsilon} = A\sigma^n$, where A and n depend on strain rate, temperature and grain size. For a fixed grain size of approximately 7 μm and temperature of 450 °C, it was observed that at slow strain rates, $\dot{\varepsilon} < 10^{-3}$ s^{-1}, the stress exponent has a value $n \approx 2.7$, while at fast strain rates, $\dot{\varepsilon} > 10^{-3}$ s^{-1}, $n \approx 4$. This suggests a transition in deformation mechanism at a strain rate around $\dot{\varepsilon} \approx 10^{-3}$ s^{-1}. Further indirect evidence for a mechanism transition is obtained from texture measurements, which show that at slow strain rates the texture remains random; at fast strain rates a strong texture develops (Ref 13). This suggests that grain-boundary sliding is the dominant deformation mechanism at slow strain rates, while solute-drag creep dominates at fast strain rates.

With an appropriate choice of constitutive parameters, the simulations predict behavior that is in good qualitative and quantitative agreement with experimental measurements. The simulations predict a transition in deformation mechanism from grain-boundary-diffusion-mediated sliding at slow strain rates, to solute drag dislocation creep, assisted by grain-boundary sliding, at fast strain rates. The mechanism transition leads to a transition in rate sensitivity that matches qualitatively the experimental measurements, but the simulations overestimate the rate sensitivity at slow strain rates. In addition, the computations have been used to predict the influence of grain size on the constitutive behavior of the alloy and have obtained good agreement with experiments.

The remainder of this paper is organized as follows. In the next section, the experimental procedures are summarized, and the computational model is outlined in Section 3. The results of our experiments are compared with the predictions of numerical simulations in Section 4, and Section 5 contains conclusions.

2. Experimental Procedure

The numerical simulations are compared with previously published experimental work on AA5083 (Ref 12). The data used represents material taken from two different steps in the rolling process, as "hot band" after warm rolling to 4.8 mm, and then after cold rolling the same material to 1.2 mm. The two materials had recrystallized grain sizes of 10 μm and 7 μm, respectively. The grain sizes were measured using the method described in ASTM standard E112. Tensile testing of the AA5083 materials was performed with the rolling direction of the sheet oriented parallel to the tensile axis. The results used for comparison in the present study were taken from strain-rate-change (SRC) tests conducted at 450 °C (Ref 12). These tests use a series of strain rates imposed upon a single specimen, with each rate held for a minimum of 2% engineering strain, to produce data for flow stress as a function of temperature, strain, and strain rate. "Steady-state" flow stress measurements were made after each rate change by evaluating the stress transient following the rate change and measuring the stress at which the transient had fully decayed. Each SRC specimen was initially pre-strained to approximately 15% engineering strain to ensure that the specimen was well seated in the grips and that its microstructure had stabilized.

Samples for electron backscatter diffraction (EBSD) studies were taken from the gauge section of tensile specimens pulled to failure at strain rates ranging from slow (3×10^{-5} s^{-1}) to fast (3×10^{-2} s^{-1}). These samples were primarily examined in the region near the failure surface. For EBSD, the sample was mounted so that the width of the gauge section was exposed. Specimen preparation techniques for EBSD are described elsewhere (Ref 13). EBSD maps were taken along the length of the gauge section starting from the failure end. The individual maps were then stitched together using software to create an image of a large area in the sample. From these maps, subset areas were selected to obtain the texture intensity values in any particular region. For all of the EBSD research, hardware and software developed by HKL, Inc. was used. This instrumentation was mounted on a JEOL 845 scanning electron microscope. A 60° tilt was used during data collection.

3. Numerical Simulation

A two-dimensional finite element method has been developed to simulate the constitutive response and deformation mechanisms in a polycrystalline aluminum alloy during quick plastic forming. The computation accounts for three processes that contribute to plastic flow: (i) dislocation creep within grains; (ii) grain-boundary sliding; and (iii) grain-boundary diffusion. In this section, the assumptions and constitutive equations used to characterize these processes are described. The numerical method is described in detail in Ref 14, so only a brief summary is given here.

A representative region of the microstructure is idealized (taken directly from a micrograph) as a two-dimensional assembly of grains, as illustrated in Fig. 1. This microstructure was used to calculate the grain size used for simulations. The grain size was calculated by taking an average of several intercept lengths in both x and y directions. The grains are represented as face-centered cubic single crystals, which deform by thermally-activated dislocation creep. The grains
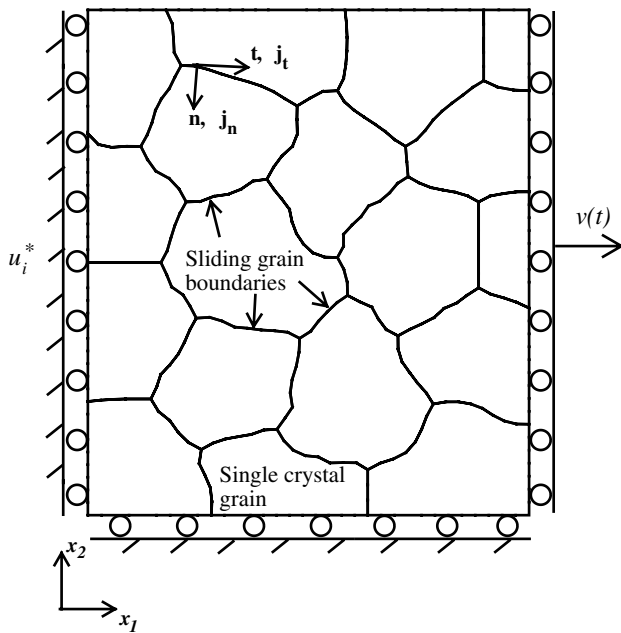
Fig. 1 Schematic of microstructure used in FEM simulations

are separated by sharp grain boundaries, which provide paths for grain-boundary diffusion and allow neighboring grains to slide with respect to one another. The material is subjected to boundary loading that is intended to approximate plane-strain uniaxial tension. Symmetry conditions are applied on boundaries at $x_2 = 0$ and $x_1 = 0$; the top surface of the microstructure, $x_2 = h$, is taken to be free of traction; and the solid is subjected to a constant strain rate of $\dot{\varepsilon}_{11} = \dot{\varepsilon}^\infty$ by displacing the boundary at $x_1 = L$. The principal objectives are to compute the displacement field u_i and stress field σ_{ij} in the solid and, in particular, to determine the average stress σ_{11} as a function of strain rate, temperature, and the grain size. In addition, the contribution to the total strain rate from each of the three inelastic deformation mechanisms is computed.

Dislocation creep within the grains is modeled using a modified form of the constitutive law for single crystals proposed by Pierce, Asaro and Needleman (Ref 15). The strain rate in the grain is decomposed into elastic and plastic parts: $\dot{\varepsilon}_{ij} = \dot{\varepsilon}_{ij}^p + \dot{\varepsilon}_{ij}^e$. The elastic strain rate is computed using the usual linear-elastic constitutive equations for a cubic crystal with Young's modulus E, shear modulus μ and Poisson's ratio ν. The plastic-strain rate is computed by summing the shearing rates on the twelve (111) [110] slip systems

$$\dot{\varepsilon}_{ij}^p = \sum_{\alpha=1}^{n} \dot{\gamma}^\alpha(q^\alpha, g^\alpha) s_i^\alpha m_j^\alpha \qquad \text{(Eq 1)}$$

where $\dot{\gamma}^\alpha$ is the shear rate on slip system α; s_i^α and m_i^α denote the slip direction and slip plane normal. The shear rate is a function of the resolved shear stress $q^\alpha = s_i^\alpha \sigma_{ij} m_j^\alpha$ acting on the slip plane and the strength of the slip system g^α. A creep law proposed by Frost and Ashby (Ref 16) is used to model slip due to thermally activated dislocation climb-plus-glide:

$$\dot{\gamma}^\alpha = \dot{\gamma}_0 \text{sign}(q^\alpha) \left(\frac{q^\alpha}{\tau_0}\right)^2 \exp\left[-\frac{\Delta\Psi}{kT}\left\{1 - \left(\frac{|q^\alpha|}{g^\alpha}\right)\right\}\right] \qquad \text{(Eq 2)}$$

where $\dot{\gamma}_0$ is a characteristic slip rate, τ_0 is the initial slip system strength, $\Delta\Psi$ is the activation energy for dislocations to escape pinning points, T is the temperature and k is the Boltzmann constant. Following Frost and Ashby, the activation energy is assumed to vary with temperature as:

$$\Delta\Psi = \Delta\Psi_0 \left(1 + \frac{300 - T}{2T_M}\right) \qquad \text{(Eq 3)}$$

where T_M is the solid's melting temperature, and $\Delta\Psi_0$ is the activation energy at $T = 300$ K. This representation is not fully consistent with experimental observations of solute-drag creep. It is, however, used as a reasonable approximation of behavior until a better representation becomes available.

At time $t = 0$, all slip systems have strength $g^\alpha = \tau_0$, which thereafter increases with plastic shearing. The Pierce, Asaro and Needleman's (Ref 15) constitutive law is used to characterize strain hardening:

$$\dot{g}^\alpha = \sum_{\beta=1}^{n} h_{\alpha\beta} |\dot{\gamma}^\beta| \qquad \text{(Eq 4)}$$

where $\dot{\gamma}^\beta$ is shearing rate on slip system β, $h_{\alpha\beta}$ is a hardening matrix, where the self-hardening modulus is given by

$$h_{\alpha\alpha} = h_0 \text{sech}^2 \left|\frac{h_0 \gamma}{\tau_s - \tau_0}\right| \text{(no sum on } \alpha) \qquad \text{(Eq 5)}$$

Here, h_0 is the initial hardening modulus, τ_0 is the initial yield stress, τ_s is the stage I stress (the stress at which large plastic flow initiates), and γ is the accumulated shear strain on all slip systems

$$\gamma = \int_0^t \sum_\alpha |\dot{\gamma}^\alpha| dt \qquad \text{(Eq 6)}$$

The latent hardening moduli are given by

$$h_{\alpha\beta} = \theta \sec h^2 \left|\frac{h_0 \gamma}{\tau_s - \tau_0}\right| \quad (\alpha \neq \beta) \qquad \text{(Eq 7)}$$

where θ is a material parameter.

An outline for modeling deformation mechanisms associated with grain boundaries is developed in this section. A representative grain boundary is sketched in Fig. 2: in the following s will denote arc length measured from some convenient point on a representative boundary, while **t** and **n** denote unit vectors tangent and normal to the boundary. The grain boundaries allow two neighboring grains to slide with respect to one another and provide a path for mass transport. Grain-boundary sliding is assumed to be a thermally-activated process, which is driven by shear tractions $\sigma_t = \sigma_{ij} t_i n_j$ acting on the grain boundary. A linear-viscous constitutive equation is used to relate the relative sliding velocity of two adjacent grains to the resolved shear stress:

$$[v_t] = (\dot{u}_i^+ - \dot{u}_i^-) t_i = \frac{\Omega\eta_0 \exp(-Q_{GBs}/kT)}{kT} \sigma_t \qquad \text{(Eq 8)}$$
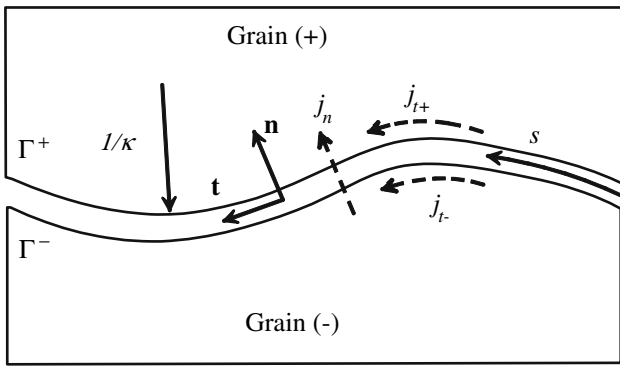
Fig. 2 Schematic of a grain boundary, showing notation and sign convention

Here, η_0 is a characteristic sliding velocity, Ω is the atomic volume, and Q_{GBs} is the activation energy for grain-boundary sliding.

Grain-boundary diffusion is driven mainly by the normal stress $\sigma_n = \sigma_{ij}n_in_j$ acting on the boundary. In this process, atoms detach from regions of the grain boundary that are subjected to compressive stress and migrate to regions that are under tensile stress, so as to reduce the total free energy of the system. As a result, material points in the grains adjacent to the boundary approach one another in regions of compressive stress and separate in regions of tensile stress. The resulting velocity discontinuity is related to stress by a linear diffusion law

$$[v_n] = (\dot{u}_i^+ - \dot{u}_i^-)n_i = \frac{\Omega D_{GB}\delta_{GB}\exp(-Q_{GB}/kT)}{kT}\frac{\partial^2}{\partial s^2}[-\sigma_n] \quad \text{(Eq 9)}$$

where $D_{GB}\exp(-Q_{GB}/kT)$ is the grain-boundary diffusivity, Q_{GB} is the corresponding activation energy, and δ_{GB} is the total thickness of the diffusion layer.

The material parameters used in FEM simulations are listed in Table 1. The parameters were estimated through several trials and the parameters resulting in a best fit with experimental data are listed.

The stress and displacement fields in the microstructure are calculated using the finite-element method described in detail in Bower and Wininger (Ref 14). Subsequently, the contribution to the total strain rate from dislocation creep, grain-boundary sliding and diffusion are computed from the slip rates within each grain and velocity discontinuities across grain boundaries:

$$\dot{\varepsilon}_{ij}^{\text{sliding}} = \frac{1}{V}\int_\Gamma [v_t]\frac{1}{2}\left(n_it_j + t_in_j\right)ds \qquad \dot{\varepsilon}_{ij}^{\text{diffusion}} = \frac{1}{V}\int_\Gamma [v_n]n_in_jds$$

$$\dot{\varepsilon}_{ij}^{\text{plastic}} = \frac{1}{V}\int_V \sum_\alpha \dot{\gamma}^\alpha\frac{1}{2}(s_i^j\alpha + s_j^\alpha m_i^\alpha)dV$$

$$\text{(Eq 10)}$$

where V denotes the area of the entire 2D microstructure and Γ denotes the collection of grain boundaries within V.

4. Results and Discussion

The principal objective is to systematically compare the predictions of the numerical simulations outlined in the preceding section with the results of experimental measurements described in Section 2. To this end, a brief summary of the main observations from the experiments is given.

Data from strain-rate change tests are shown in Fig. 3, and are presented as plots of the logarithm of true strain rate, $\dot{\varepsilon}$, versus true, steady-state flow stress, σ. Results are shown for specimens with recrystallized grain sizes of 7 and 10 μm. The data can be fit approximately by a phenomenological creep law of the form:

$$\dot{\varepsilon} = A\sigma^n \exp\left(\frac{-Q_C}{RT}\right) \quad \text{(Eq 11)}$$

where A is a material constant, n is the stress exponent, Q_C is the activation energy for creep, R is the universal gas constant, and T is temperature. The material constants A, n, and Q_C depend on the dominant deformation mechanism, and hence, are functions of strain rate, grain size, and temperature. The data suggest that material behavior can be classified into two distinct regimes. At fast strain rates, data can be fit with a stress exponent $n \approx 4$. In this regime, material behavior is insensitive to grain size. At slow strain rates, the sample with a smaller grain size exhibits a lower flow stress and a transition to a stress exponent of approximately 2.7, while the coarser-grained material maintains a stress exponent of $n \approx 4$ in this regime.

The change in stress exponent in the fine-grained specimens suggests a transition in deformation mechanism from dislocation creep at fast strain rates to grain-boundary-sliding creep at slow strain rates. Further evidence has been obtained for such a mechanism transition from the deformation and failure characteristics of the fine-grained (7 μm) specimens. For example, in the dislocation-creep regime, AA5083 exhibits sharp inverse creep transients upon loading or a strain-rate change, shows necking-controlled failure, and develops a strong texture with increasing strain. In contrast, when the fine-grained materials are deformed at slow strain rates (the grain-boundary-sliding regime), they show no transients upon loading or changes in
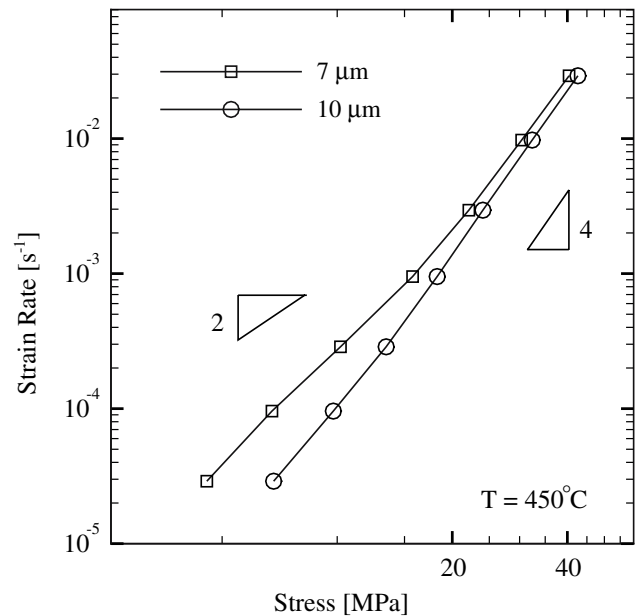

Fig. 3 Experimental data for AA5083 showing strain rate –vs.– stress at 450 °C. Data taken from Kulas et al. (Ref 12) and refers to AA5083 version DC-D in this reference

strain rate, exhibit randomization of texture with strain, and fail by cavitation rather than necking. These differences in deformation mechanism are illustrated in Fig. 4 by examining failure morphology and texture. Figure 4(a) shows that samples failed by necking at a strain rate of $0.06\ s^{-1}$ (dislocation-creep regime), while necking was not observed at a strain rate of $3 \times 10^{-4}\ s^{-1}$ (grain-boundary-sliding regime). In Fig. 4(b), the crystallographic orientations are color coded as shown. At $0.0005\ s^{-1}$ strain rate, a random distribution of colors indicates random orientation of grains or weak texture (grain-boundary-sliding regime). At $0.03\ s^{-1}$ strain rate, a majority of the grains are colored blue, indicating strong texture wherein the (100) direction is parallel to the x-axis or tensile direction.

The experimental stress–strain rate curves are compared with the predictions of numerical simulations in Fig. 5(a). The constitutive parameters used in these simulations were chosen to give the best fit with the experimental data for specimens with a grain size of 7 μm; the same material properties were then used to predict the behavior of specimens with 10 μm grain size. The simulations predict stress–strain rate curves that are in good qualitative and quantitative agreement with experimental data. The agreement between theory and experiment is particularly good in the dislocation creep regime, where the computations predict a stress exponent $n \approx 4$ that closely matches experimental data. The prediction also shows

little effect of grain size on the flow stress in this regime, which is consistent with the experimental results.

The simulations appear to underestimate the stress exponent (or equivalently to overestimate the rate sensitivity) in the grain-boundary-sliding creep regime as seen in Fig. 5(b). There are several possible explanations for this discrepancy. The computations use the simplest possible models of both grain-boundary-sliding and diffusion: a linear-viscous law is used to model grain boundary sliding; similarly, a linear diffusion law is used to model grain-boundary diffusion. These are most likely to be appropriate for pure metals. In alloys such as AA5083, grain-boundary chemistry affects the mechanical response of grain boundaries, which could be accounted for in our simulations by using reaction-controlled diffusion equations. In addition, the effects of void nucleation and growth in the computations have not been included and grain-boundary migration has been neglected. The model also did not include a threshold stress for grain-boundary sliding, which could lead to the lower strain-rate sensitivity at lower stresses. Extending the computations to account for these phenomena is a promising direction for future research.

The computations predict a creep mechanism transition that matches experimental results. The mechanism transition is illustrated in Fig. 6, which shows the predicted contribution to the total strain rate from dislocation creep, grain-boundary
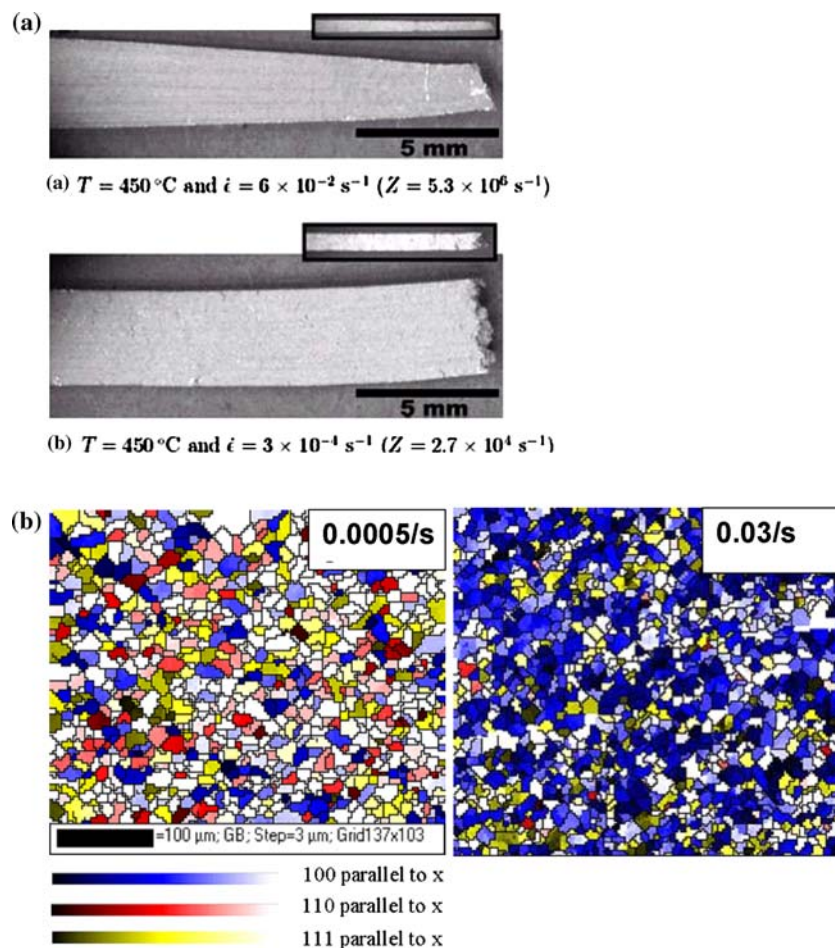

(a) $T = 450\,°C$ and $\dot{\varepsilon} = 6 \times 10^{-2}\ s^{-1}$ $(Z = 5.3 \times 10^6\ s^{-1})$

(b) $T = 450\,°C$ and $\dot{\varepsilon} = 3 \times 10^{-4}\ s^{-1}$ $(Z = 2.7 \times 10^4\ s^{-1})$

Fig. 4 Two examples of the difference between grain-boundary sliding and dislocation creep deformation mechanisms (a) fracture morphology: uniform thinning versus necking (From Ref 12) and (b) OIM texture map near failure showing random texture in GBS regime ($0.0005\ s^{-1}$) and strong texture in dislocation creep regime ($0.03\ s^{-1}$) (Ref 13)
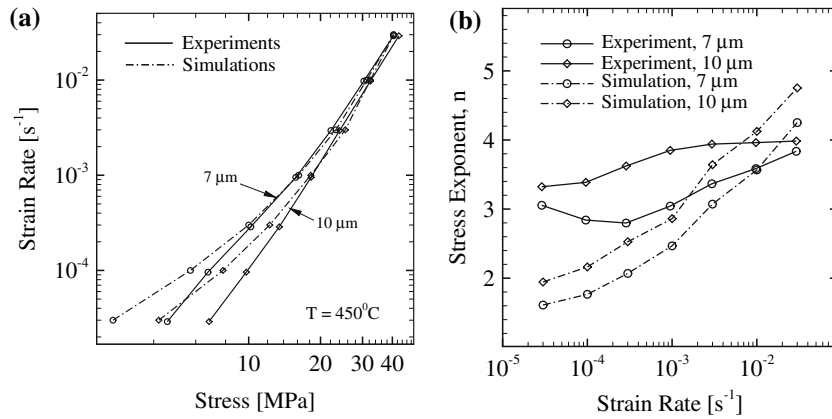
Fig. 5 (a) Comparison of experimental stress–strain rate with simulations, and (b) Stress exponent as a function of grain size and strain rate for experiment and simulation

sliding, and diffusion. At high strain rates, dislocation creep dominates, but at a strain rate of approx. 0.001 s^{-1}, the deformation mechanism transitions to a combination of grain-boundary sliding and grain-boundary diffusion. It is this transition that causes an increase in strain-rate sensitivity.

It is notable that Coble creep, (resulting from grain-boundary diffusion) is predicted to be the dominant deformation mechanism at low rates of strain. This is counter to the commonly held view that grain-boundary sliding is the dominant deformation mechanism at low rates of strain. The simulations show, however, that grain-boundary sliding is a very inefficient mechanism of deformation, because in general it results in an incompatible displacement field in the polycrystal. Consequently, grain-boundary sliding can operate only if either a substantial number of voids are present at triple junctions that can accommodate the incompatibility; or a
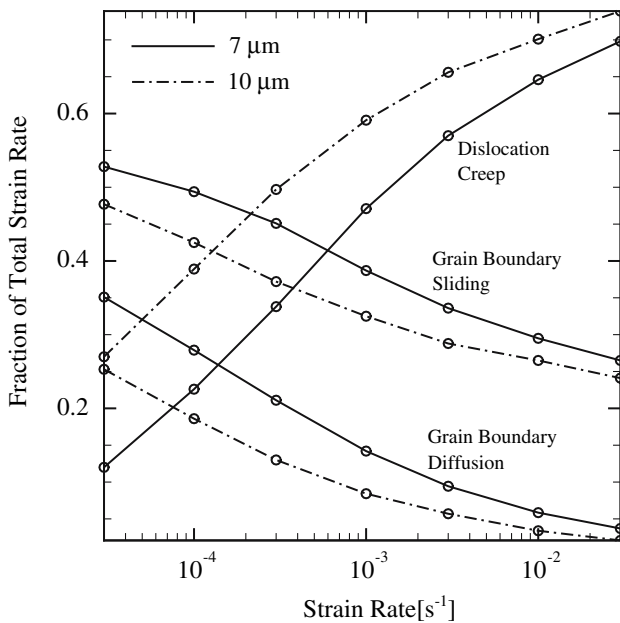
Table 1 Values for material parameters used to fit experimental data with simulations

Parameter	Value
Grain size L	7 or 10 μm
Atomic volume Ω	1.66×10^{-29} m^3
Melting temperature T_M	933 K
Young's modulus E	70 GN m^{-2}
Poisson's ratio ν	0.3
Shear modulus μ	26.9 GN m^{-2}
Characteristic strain rate $\dot{\gamma}_0$	0.42×10^6 s^{-1}
Initial yield stress τ_0	65 MN m^{-2}
Saturated yield stress τ_s	97.5 MN m^{-2}
Initial hardening rate h_0	100 MN m^{-2}
Latent hardening factor θ	1.0
Activation energy at 300 K $\Delta\psi_0$	2.97×10^{-19} J
Grain boundary diffusion pre-exponential $\delta_{GB} D_{GBt}$	9.9×10^{-14} m^3 s^{-1}
Grain boundary diffusion activation energy Q_{GBt}	1.34×10^{-19} J
Grain boundary sliding pre-exponential η_0	259.5 m s^{-1}
Grain boundary sliding activation energy Q_{GBs}	1.34×10^{-19} J

Fig. 6 Predicted contribution of dislocation creep, grain-boundary sliding, and grain-boundary diffusion to total strain rate as a function of strain rate and grain size. Results are shown for parameter values listed in Table 1

second deformation mechanism acts in combination with grain-boundary sliding. Voids have not been included in the simulations, so the incompatibility is accommodated by plastic flow within the grains at fast rates of strain, or diffusion at slow rates of strain. Although grain-boundary sliding cannot act in isolation, it does substantially increase the strain rate in both regimes. In addition, the occurrence of grain-boundary sliding shifts the transition from Coble creep to a higher strain rate, and therefore has a strong, albeit indirect, influence on rate sensitivity, and grain size dependence of flow strength.

The long-term objective of the research presented in this paper is to contribute to efforts to develop alloys with improved hot formability by means of appropriate modifications in alloy composition or microstructure. As a preliminary step towards this goal, numerical simulations have been used to predict the influence of the material parameters that govern microscopic processes that control deformation in the alloy. The computations account for three primary mechanisms of deformation: dislocation creep within grains, grain-boundary sliding, and grain-boundary diffusion. Dislocation creep is modeled using the phenomenological constitutive equation (2) proposed by Frost and Ashby (Ref 16), which assumes that plastic flow
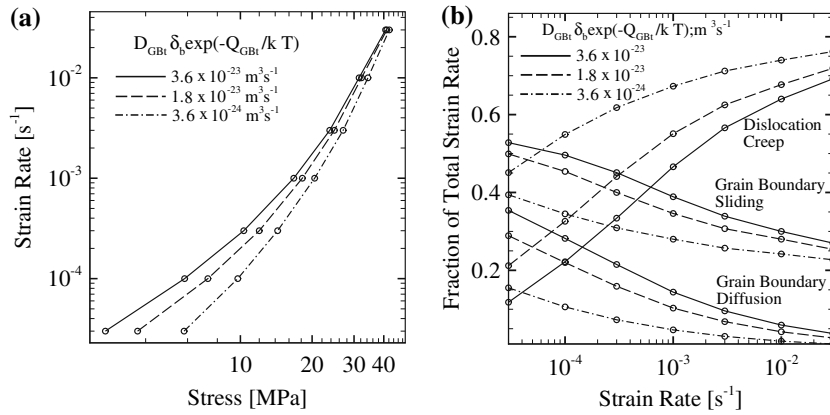
Fig. 7 (a) Effect of diffusivity on stress and (b) effect of diffusivity on mechanism transition. Results are for $\tau_0 = 70$ MPa, $\tau_s = 105$ MPa, with remaining parameters as given in Table 1

occurs by a thermally activated process involving dislocations escaping from pinning obstacles. Although a large number of material parameters appear in our constitutive equations, it has been shown that, for loading conditions of interest, only four parameters have a major effect on the strain-rate response of the alloy: the grain-boundary diffusivity $D_{GB}\delta_{GB}\exp(-Q_{GB}/kT)$, the grain-boundary sliding constant $\eta_0\exp(-Q_{GBs}/kT)$ the rate constant for dislocation creep $\dot{\gamma}_0$ and the plastic flow strength τ_o. The influence of these parameters is illustrated in Figs. 7–10. Parameter values for these simulations are listed in Table 1, unless specified otherwise in the figure captions. The following trends are observed:

(i) The effects of varying grain-boundary diffusion are illustrated in Fig. 7. Decreasing the diffusivity leads to a slower strain-rate contribution by grain-boundary diffusion and grain-boundary sliding, making dislocation creep the dominant mechanism of deformation at slow strain rates. As a result, the stresses at slow strain rates are higher for slower diffusivities, as shown in Fig. 7(a). As diffusivity decreases, the transition from dislocation creep to grain-boundary sliding moves to slower strain rates, as shown in Fig. 7(b).

(ii) The effects of varying the rate constant $\dot{\gamma}_0$ are illustrated in Fig. 8. As the rate constant $\dot{\gamma}_0$ increases, the stress–strain rate curve is shifted on the strain-rate axis towards faster strain rates or, equivalently, results in lower stresses at a given strain rate. The transition in deformation mechanism from dislocation creep to grain-boundary sliding and diffusion also moves to slower strain rate.

(iii) In Fig. 9, the flow strength, τ_o and rate constant, $\dot{\gamma}_0$, are varied simultaneously, to keep the ratio $\dot{\gamma}_0/\tau_0^2$ constant while varying τ_o. As a result, τ_0 influences behavior only through its influence on the breakdown slip strength g^α in the exponential term in eq. (2). Figure 9 shows that changing τ_o and $\dot{\gamma}_0$ in this way has only a minor influence on stress, such that decreasing τ_o reduces the stress slightly at fast strain rates. This shows that the stresses in the grains only reach the breakdown regime when the solid is loaded at fast strain rates, and otherwise deform predominantly by thermally activated dislocation motion.

(iv) The influence of grain-boundary sliding constant $\eta_0\exp(-Q_{GBs}/kT)$ is illustrated in Fig. 10. Grain-boundary sliding is modeled in our simulations using a linear–viscous constitutive eq. (8), proposed by Raj and Ashby (Ref 17). In this model, grain-boundary sliding occurs by microscopic diffusion on the grain boundary, so that
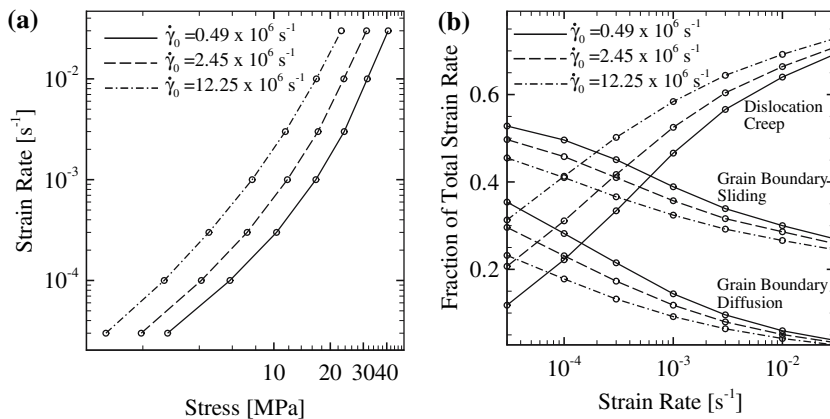

Fig. 8 (a) Effect of rate constant on stress and (b) effect of rate constant on mechanism transition. Results are for $\tau_0 = 70$ MPa, $\tau_s = 105$ MPa, with remaining parameters as given in Table 1
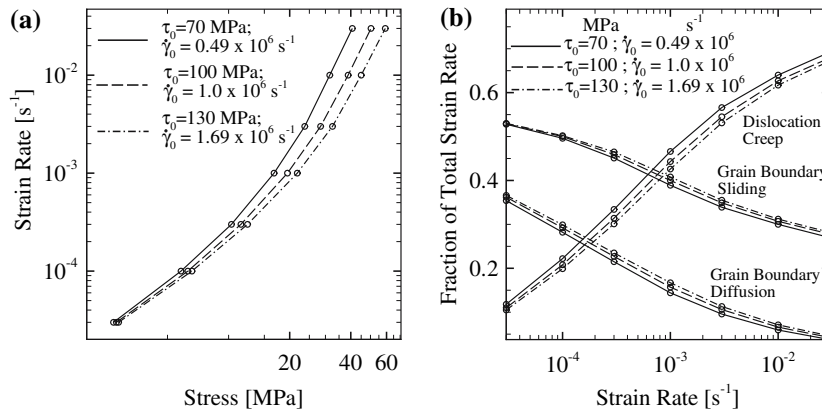
Fig. 9 (a) Effect of initial flow strength on stress and (b) effect of initial strength on mechanism transition. Results are for τ_s = 105, 150 and 195 MPa for τ_0 = 70, 100 and 130 MPa respectively, with remaining parameters as given in Table 1
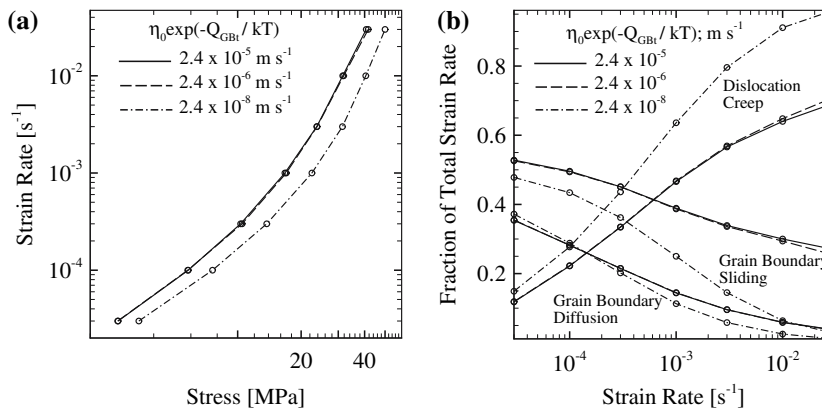

Fig. 10 (a) Effect of grain-boundary-sliding rate constant $\eta_0 \exp(-Q_{GBt}/kT)$ on stress and (b) effect of grain-boundary-sliding rate on mechanism transition. Results are shown for τ_0 = 70 MPa, τ_s = 105 MPa, and other parameters are as given in Table 1

the characteristic sliding velocity, $\eta_0 \exp(-Q_{GBs}/kT)$, is related to the diffusivity of the grain boundary, $D_b \delta_b \exp(-Q_{GB}/kT)$, and the amplitude of grain boundary roughness, r, through $\eta_0 \exp(-Q_{GBs}/kT) = 8(D_b \delta_b / r^2) \exp(-Q_{GB}/kT)$. This equation has been used to estimate values for viscosity: the results are given in Table 1. With representative values for diffusivity and roughness, our simulations predict that grain-boundary sliding is active at both fast and slow strain rates. Consequently, varying the sliding rate within practical ranges does not have any significant effect on the behavior of the solid. The sliding rate constant only has an effect when it is decreased to very low values, in which case grain-boundary sliding is suppressed, which also substantially reduces diffusional creep, as shown in Fig. 10. The values used for matching experimental data to simulations are much higher than these values.

These studies suggest that the rates of dislocation creep and grain-boundary diffusion should have the greatest influence on formability. Increasing the rate of grain-boundary diffusion, and decreasing the rate of dislocation creep will shift the transition in deformation mechanism to higher strain rates, and increase strain-rate sensitivity. Both these changes in material response should improve formability.

5. Conclusions

1. A finite element method which incorporates grain-boundary diffusion, grain-boundary sliding, and dislocation creep has been developed and used to model experimental results with AA5083.
2. Good qualitative and quantitative correlation between the model and experimental results for strain rate vs. stress behavior was observed.

   a. Excellent correlation was observed in the dislocation creep regime both in terms of flow stress and strain-rate sensitivity, and the insensitivity to grain size.
   b. The model overpredicts the strain-rate sensitivity and underpredicts the flow stress in the grain-boundary-sliding regime. This is likely due to the grain boundary differences between a pure metal (as modeled) and an engineering alloy.
   c. The relative effect of grain size on flow stress and the transition between grain-boundary sliding and dislocation creep was accurately modeled.

3. A sensitivity analysis of key parameters in the model showed that diffusivity, the rate constant and strength had

the largest effects on the deformation mechanism and constitutive behavior of the solid.

References

1. A.J. Barnes, Superplastic Forming of Aluminum Alloys, *Mater. Sci. Forum*, 1994, **170-172**, p 701–714
2. J.G. Schroth, "General Motors Quick Plastic Forming process," *Advances in Superplasticity and Superplastic Forming*, E.M. Taleff, P.A. Friedman, P.E. Krajewski, R.S. Mishra, and J.G. Schroth, Eds., TMS, 2004, p 9–20
3. R. Verma, A.K. Ghosh, S. Kim, and C. Kim, Grain Refinement and Superplasticity in 5083 Al, *Mater. Sci. Eng. A*, 1995, **191**, p 143–150
4. R. Verma, P.A. Friedman, A.K. Ghosh, S. Kim, and C. Kim, Characterization of Superplastic Deformation Behavior of a Fine Grain 5083 Al Alloy Sheet, *Metall. Mater. Trans. A*, 1996, **27A**, p 1889–1898
5. M.A. Khaleel, M.T. Smith, and S.G. Pitman, The Effect of Strain Rate History on the Ductility in Superplastic AA-5083, *Scripta Mater.*, 1997, **37**(12), p 1909–1915
6. H. Iwasaki, H. Hosokawa, T. Mori, T. Tagata, and K. Higashi, Quantitative Assessment of Superplastic Deformation Behavior in a Commercial 5083 Alloy, *Mater. Sci. Eng. A*, 1998, **252**, p 199–202
7. S.N. Patankar and T.M. Jen, Strain Rate Insensitive Plasticity in Aluminum Alloy 5083, *Scripta Mater.*, 1998, **38**(8), p 1255–1261
8. I.C. Hsiao and J.C. Huang, Development of Low Temperature Superplasticity in Commercial 5083 Al-Mg Alloys, *Scripta Mater.*, 1999, **40**(6), p 697–703
9. C.F. Martin, J.J. Blandin, and L. Salvo, Variations in Microstructure and Texture during High Temperature Deformation of Al–Mg Alloy, *Mater. Sci. Eng. A*, 2001, **297**, p 212–222
10. R.M. Cleveland, A.K. Ghosh, and J.R. Bradley, Comparison of Superplastic Behavior in Two 5083 Aluminum Alloys, *Mater. Sci. Eng. A.*, 2003, **351**(1–2), p 228–236
11. O.D. Sherby and J. Wadsworth, Superplasticity-Recent Advances and Future Directions, *Prog. Mater. Sci.*, 1989, **33**, p 169–221
12. M.-A. Kulas, W.P. Green, E.M. Taleff, P.E. Krajewski, and T.R. McNelley, Deformation Mechanisms in Superplastic AA5083 Materials, *Metall. Mater. Trans. A*, 2005, **36**(5), p 1249–1261
13. S. Agarwal, P.E. Krajewski, and C.L. Briant, Texture Development and Dynamic Recrystallization in AA5083 during Superplastic Forming at Various Strain Rates, *Advances in Superplasticity and Superplastic Forming*, E.M. Taleff, P.A. Friedman, P.E. Krajewski, R.S. Mishra, and J.G. Schroth, Eds. Charlotte, TMS, 2004, p 95–108
14. A.F. Bower and E. Wininger, A Two-Dimensional Finite Element Method for Simulating the Constitutive Response and Microstructure of Polycrystals during High-Temperature Plastic Deformation, *J. Mech. Phys. Solids*, 2004, **52**, p 1289–1317
15. D. Pierce, R.J. Asaro, and A. Needleman, Material Rate Dependence and Localized Deformation in Crystalline Solids, *Acta Metall.*, 1983, **31**, p 1951–1976
16. H. Frost, M.F. Ashby, *Deformation Mechanism Maps*, 1st ed., Chap. 4, Pergamon Press, 1982, p 20–29
17. R. Raj and M.F. Ashby, On Grain Boundary Sliding and Diffusion Creep, *Metal. Trans.*, 1971, **2**(4), p 1113–1127